Accepted Manuscript

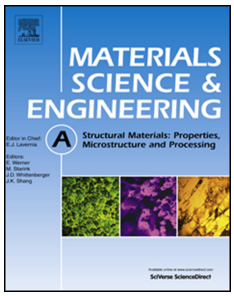

Additive manufacturing of fine-grained and dislocation-populated CrMnFeCoNi high entropy alloy by laser engineered net shaping

S. Guan, D. Wan, K. Solberg, F. Berto, T. Welo, T.M. Yue, K.C. Chan

PII: S0921-5093(19)30842-1

DOI: https://doi.org/10.1016/j.msea.2019.138056

Article Number: 138056

Reference: MSA 138056

To appear in: *Materials Science & Engineering A*

Received Date: 18 February 2019

Revised Date: 19 June 2019

Accepted Date: 20 June 2019

Please cite this article as: S. Guan, D. Wan, K. Solberg, F. Berto, T. Welo, T.M. Yue, K.C. Chan, Additive manufacturing of fine-grained and dislocation-populated CrMnFeCoNi high entropy alloy by laser engineered net shaping, *Materials Science & Engineering A* (2019), doi: https://doi.org/10.1016/j.msea.2019.138056.

Additive manufacturing of fine-grained and dislocation-populated CrMnFeCoNi high entropy alloy by laser engineered net shaping

S. Guan [a], D. Wan [b], K. Solberg [b], F. Berto [b], T. Welo [b], T.M. Yue [a], K.C. Chan [a,*]

a Advanced Manufacturing Technology Research Center, Department of Industrial and Systems Engineering, The Hong Kong Polytechnic University, Hung Hom, Kowloon, Hong Kong

b Department of Mechanical and Industrial Engineering, Norwegian University of Science and Technology, Richard Birkelands vei 2B, 7491 Trondheim, Norway

* Corresponding author.

Email address: kc.chan@polyu.edu.hk (K.C. Chan)

Abstract:

The equiatomic CrMnFeCoNi high entropy alloy is additively manufactured by the laser engineered net shaping (LENS^{TM}) process, and the solidification conditions, phase formation, as-deposited microstructures, and tensile behavior are investigated. The LENS^{TM}-deposited CrMnFeCoNi alloy exhibits a single-phase disordered face centered cubic (FCC) structure, as evidenced by X-ray diffraction (XRD), and rationalized by Scheil's solidification simulation. Furthermore, microstructures at multiple length scales, i.e. columnar grains, solidification substructures, and dislocation substructures, are formed. The tensile deformation process is mainly accommodated by dislocation activities with the assistance of deformation twinning. The tensile yield strength of the LENS^{TM}-deposited CrMnFeCoNi alloy is comparable to that of finer-grained wrought-annealed counterparts, due to the additional initial-dislocation strengthening. However, the uniform tensile elongation, by contrast, is lowered, which is attributed to the increased dynamic dislocation recovery rate and

hence the weakened work hardening capability of the LENS^{TM}-deposited CrMnFeCoNi. This study demonstrates the capability of the LENS^{TM} process for manufacturing the CrMnFeCoNi alloy, with high performance, for engineering applications.

Keywords: Additive manufacturing; CrMnFeCoNi high entropy alloy; Multi-scale as-deposited microstructure; Strengthening mechanism; Dislocation strengthening; Ductility

1. Introduction

Conventional alloys contain one dominant element as the base metal, such as Fe in steels, with minor addition of alloying elements to tune the microstructures and properties. This traditional alloy design philosophy has been challenged since high entropy alloys (HEAs) were introduced in 2004, comprising multi-principal elements with each at a concentration of 5 ~ 35 at.% [1, 2]. This new alloy design strategy vastly expands the range of possible alloy systems, and therefore increase the possibilities for discovering improved properties such as high strength [3-5] and excellent fatigue performance [6, 7]. Among a vast variety of possible alloy systems, the equiatomic CrMnFeCoNi alloy has received more attention due to its excellent ductility and extraordinary damage tolerance, especially at cryogenic temperatures [8-10]. For instance, its fracture toughness value, at liquid-nitrogen temperature, exceeds 200 MPa·m$^{1/2}$, that is superior to most metal alloys [10].

To date, however, the majority of CrMnFeCoNi alloys are manufactured by casting processes and are therefore dominated by coarse-grained (CG, up to hundreds of micrometers) microstructures that produce low yield stress [11]. To achieve

fine-grained (FG, 500 nm to a dozen or so micrometers) microstructures, complex cold forging and/or rolling and subsequent annealing processes are normally needed [8, 10]. Some severe plastic deformation (SPD) techniques (e.g. high pressure torsion, HPT) and mechanical alloying have even been used to prepare the bulk CrMnFeCoNi alloys with ultrafine-grained (UFG, < 500 nm) or even nanocrystalline (NC, < 100 nm) microstructures [12-15]. The UFG/NC CrMnFeCoNi alloys are strengthened effectively, possibly due to the nanoscale and interfacial effects, but the uniform tensile ductility decreases dramatically below a few per cent, or even approaching zero [14, 15]. Details of the nanoscale and interfacial effects have been discussed in [16]. The reduced ductility can be attributed to the weakened capacity for sustainable work hardening, and thus the early formation of necking that terminates the uniform plastic deformation [16-18]. Overall, a good combination of the tensile yield strength and useful uniform elongation is currently achieved in the FG regime. However, conventional metallurgical routes (e.g. cold-deformation and subsequent annealing) enabling the achievement of FG microstructures are relatively complex. Furthermore, only simple geometries can be achieved, and normally post machining is required. All these disadvantages are intrinsic to these conventional routes, and it is therefore difficult or even impossible to avoid.

Additive manufacturing (AM) increases the design and manufacturing flexibilities and therefore has great potential for applications in the metal manufacturing industry. Components with complex geometries can be near-net-shaped by the AM process and no post machining is required. Furthermore, dies are not needed for the AM process. In addition to the above-mentioned advantages, the AM process has the potential to achieve uniquely fine as-solidified microstructures due to the rapid cooling effects [19-21]. This enables the AM process

to manufacture complex shaped components and prepare FG microstructures in a single-step, which are not accessible in conventional metallurgical processes. Selective laser melting (SLM), a very popular laser powder-bed-fusion (PBF) AM process, has been used to print the CrMnFeCoNi alloy, with a good combination of strength and ductility [22-24]. The laser powder-blown AM process has also been employed to manufacture the CrMnFeCoNi alloys. Some of the powder-blown AM-ed CrMnFeCoNi alloys are not strong enough [11, 25, 26], maybe due to the inappropriate processing parameters and thus the coarse microstructures. Recently, a good combination of strength and ductility has been also achieved in the powder-blown AM-ed CrMnFeCoNi alloys [27, 28]. However, a more systematic investigation is needed to better understand the solidification conditions, microstructural formation and tensile behavior of the AM-ed CrMnFeCoNi alloy.

In this study, the CrMnFeCoNi alloy is additively manufactured by the laser engineered net shaping (LENS^{TM}) process, that also adopts the powder feeding mechanism. The solidification conditions, phase formation, as-deposited microstructures, and tensile behavior of the LENS^{TM}-deposited CrMnFeCoNi alloy are investigated, and its tensile properties are compared with various CrMnFeCoNi alloys processed by conventional and alternative AM processes. The strengthening mechanisms and the origin of reduced ductility, as compared with the wrought-annealed counterparts, are discussed.

2. Experimental procedure

2.1. Specimen fabrication by the LENS^{TM} process

The CrMnFeCoNi specimen was manufactured on the LENS^{TM} MR-7 system, which is schematically shown in Fig. 1 (a). The CrMnFeCoNi prealloyed powders

with equiatomic compositions were prepared by the plasma rotating electrode process (PREP) and were loaded in the powder hopper. The powders were injected, with the aid of the flowing argon gas, into the powder delivery line, then to the powder feed nozzles and finally to the melt pool that was created by a high-powered laser beam with a focus diameter of approximately 600 μm. The specimen was deposited onto an austenitic 316L stainless steel substrate. The laser beam was scanned in a zigzag way (i.e. the bidirectional scan), and a 90° rotation of the scan direction (i.e. the cross-hatched scan) was used between consecutive layers, as shown in Fig. 1 (b). Before building the tensile specimen, we performed a series of control experiments by building small CrMnFeCoNi samples (10 mm by 10 mm by 8 mm) and based on the minimum defects criterion, the following optimized parameters were used for depositing the specimen for tensile testing: a laser power of 400 W, a scan speed of 5 mm/s, a linear heat input (i.e. the applied laser power divided by the laser scan speed) of 80 J/mm, and a hatch spacing of 460 μm. During the fabrication, the melt pool was monitored by the ThermaViz system, which incorporates a two-wavelength imaging pyrometer as well as image acquisition and analysis software (Fig. 1 (a)). The two-color or ratio pyrometer measures in two spectral ranges simultaneously and determines the temperature by calculating the radiation ratio. The imaging pyrometer was calibrated using a high-temperature tungsten filament before use, and can provide real-time (25 frames/second) and high resolution (12.1 μm/pixel) temperature measurements over a wide range of temperatures from 1273 to 3073 K. From these temperature data, we can calculate the solidification conditions, e.g. the thermal gradient and cooling rate, which are critical for the microstructural formation. Moreover, the whole fabrication process was carried out in an enclosed chamber with the oxygen level below 20 parts per million (ppm) to minimize any potential

oxidation.

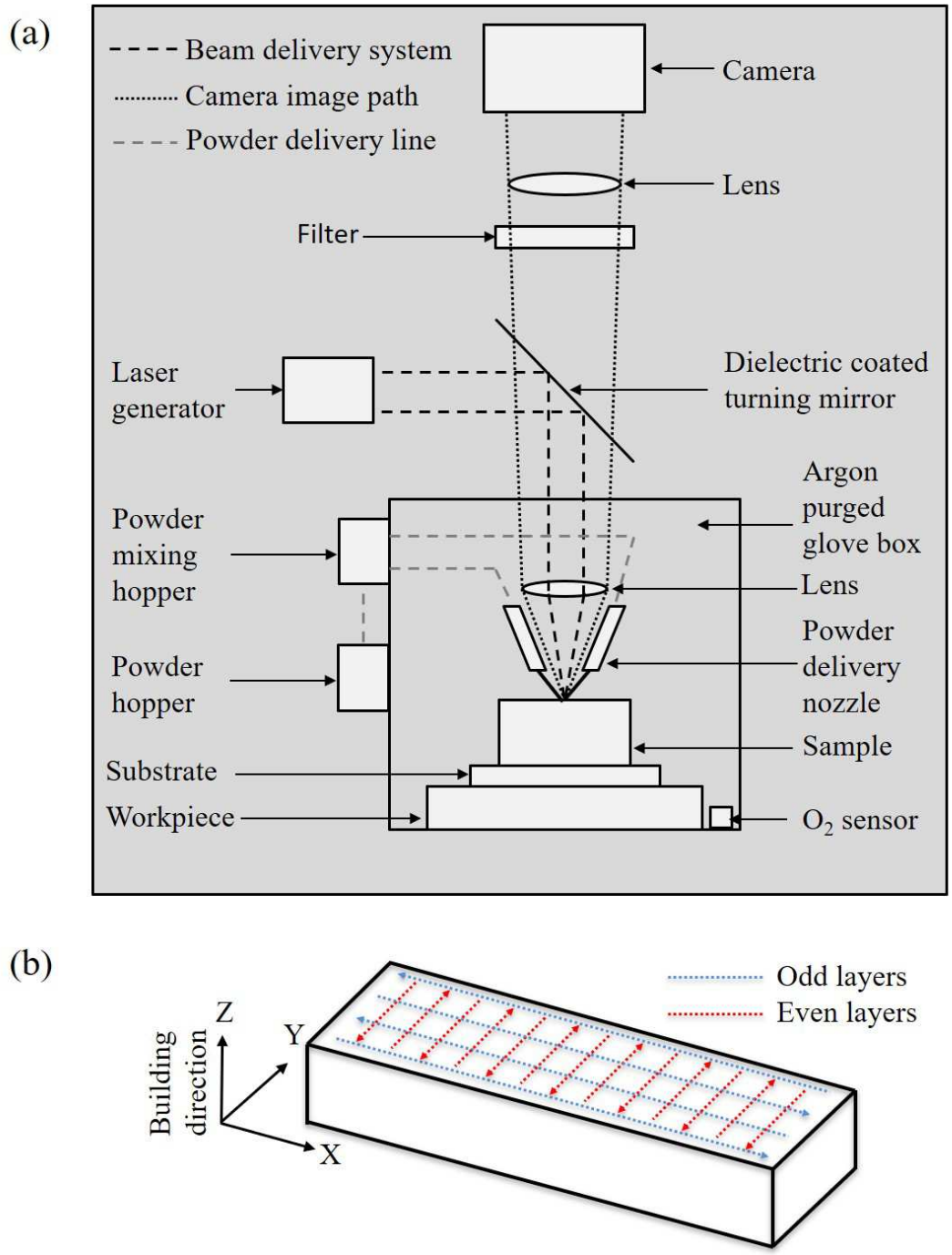

Fig. 1. (a) Schematic of the LENS^{TM} MR-7 System; (b) Schematic of the laser scan pattern showing the bidirectional and cross-hatched scan strategy. The blue and red arrows indicate the laser scan direction for odd and even layers, respectively. The building direction Z is aligned vertically upwards.

2.2. Material characterization

The density of the LENS^{TM}-deposited specimen was measured by the Archimedes method. The internal defects inside the LENS^{TM}-deposited specimen were examined by the dual-tube micro-focus X-ray computed tomography (CT) System YXLON FF35 CT, operating at a tube voltage of 150 kV and a tube current of 60 μA. During CT examination, the specimen was rotated from 0° to 360° with an increment of 0.2°, and a total of 1800 projections were generated in a full rotation and then reconstructed to achieve the 3D information of the internal defects. The current operating mode enables us to detect the internal defects down to 3 μm. The residual stress (in-plane stress σ_x) in the LENS^{TM}-deposited specimen was measured on a X-ray diffractometer with a Cr Kα radiation. The diffraction angle 2θ = 128° for the {220} crystal plane family was used to have high diffraction peak, and the residual stress value was calculated by $sin^2\varphi$ method.

The tensile test was carried out on a servo-hydraulic 810 Material Test System (MTS), at room temperature, with an engineering strain rate of 10^{-3} s^{-1}. Rectangular dog-bone shaped specimens, for tensile testing, were machined from the LENS^{TM}-deposited specimen, with their longitudinal axes (i.e. tensile axis) along the X direction. The gauge length of the tensile specimen was 10 mm, and the gauge width and gauge thickness were 3 and 0.9 mm, respectively, after final polishing. Microstructural analysis before and after the tensile test was performed with the aid of X-ray diffraction (XRD), optical microscopy (OM), scanning electron microscopy (SEM) equipped with energy dispersive X-ray spectroscopy (EDS) and electron backscatter diffraction (EBSD), and electron channeling contrast imaging (ECCI) techniques. The XRD examination was performed on a Rigaku SmartLab X-ray diffractometer, with a Cu Kα source scanning from 30° to 100° at a scan rate of

5 °/min. The SEM, EDS, and EBSD investigations were conducted in a Quanta 650 SEM (Thermo Fisher Scientific Inc., USA) with an acceleration voltage of 20 kV, and the ECCI investigation was done in the same microscope, but with an increased acceleration voltage of 30 kV. Samples for SEM, EDS, EBSD, and ECCI investigations were cut from the LENS^{TM}-deposited specimen by electrical discharge machining (EDM), and then successively ground with emery papers up to 4000 grit size, and finally polished with diamond suspension and colloidal silica-based slurry down to 0.05 μm particle size. The specimen for OM examination was electrolytically etched, after mechanical grinding and polishing, in a solution of 10% HNO_3, 5% $C_2H_4O_2$, and 85% H_2O. Furthermore, the solidification path and solidification segregation of the CrMnFeCoNi alloy were simulated by Scheil's model with the aid of Thermo-Calc software and TCHEA v2.0 high entropy alloys thermodynamic database. The simulated results by Scheil's model were based on the basic assumptions of no diffusion in the solids and infinite diffusion in the liquids.

3. Results

3.1. Densification

The density of the LENS^{TM}-deposited CrMnFeCoNi alloy was measured to be 7.953 g/cm^3 by the Archimedes method, leading to a relative density of 99.67% (assuming the theoretical density of the CrMnFeCoNi alloy is 7.980 g/cm^3). Fig. 2 (a)-(d) give the X-ray CT 2D and 3D images of the LENS^{TM}-deposited CrMnFeCoNi alloy, also showing no obvious pores and thus very dense specimen. Based on the X-ray CT data, the porosity (i.e. defect volume ratio) was determined to be 0.25%, indicating a relative density of 99.75%. This value is slightly higher than the relative density value determined by the Archimedes method because some very small pores

cannot be detected by X-ray CT due to its resolution restriction. Fig. 2 (e) shows the pore size distribution in the LENS^{TM}-deposited CrMnFeCoNi alloy. It can be seen that the pore size follows a normal distribution, and the average size of the pores is approximately 6 μm. Most importantly, no extremely large pores were detected, which are definitely detrimental to the ductility.

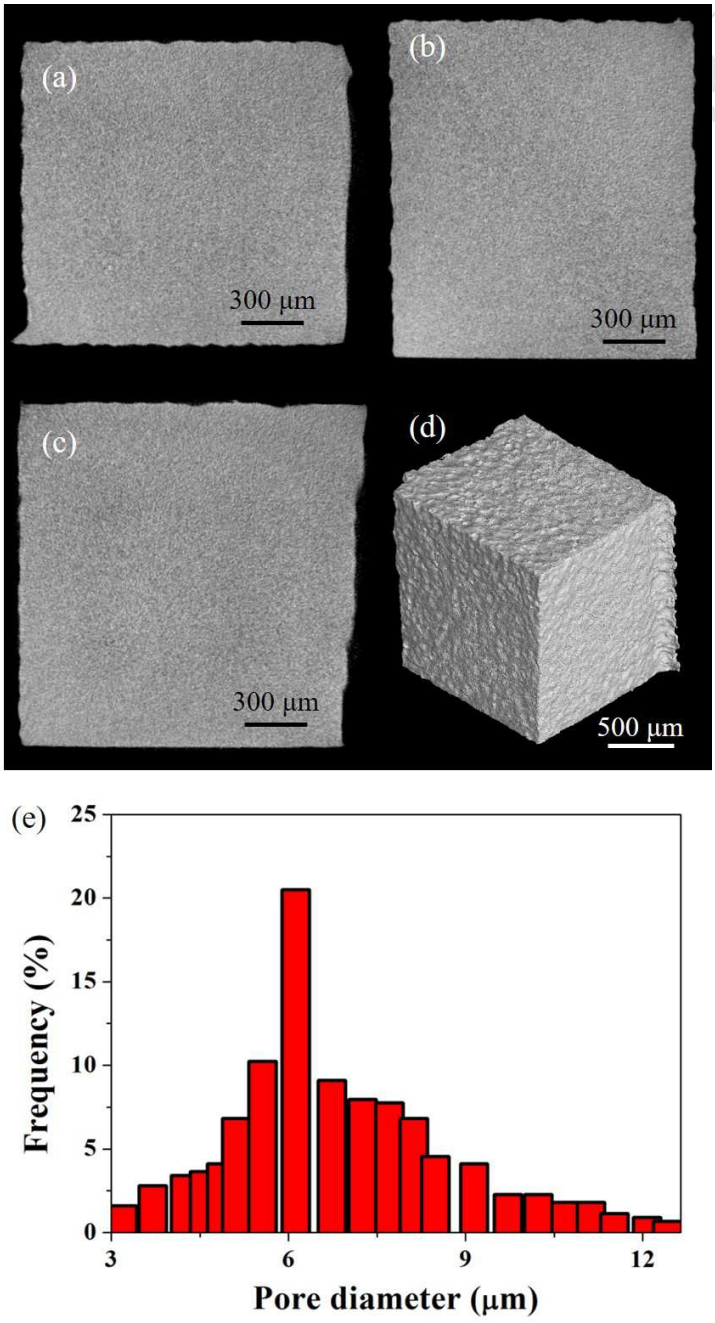

Fig. 2. X-ray CT characterization of internal pores in the LENS^{TM}-deposited

CrMnFeCoNi alloy. (a) Top view; (b) Right view; (c) Front view; (d) 3D view; (e) Pore size distribution.

3.2. Solidification conditions

Fig. 3 (a) gives a typical thermal map of the melt pool looking down from the top during the LENS^{TM} processing, with the laser scan direction indicated by the white arrow. The map was colorized to show the temperature (in Kelvin) down to the liquidus temperature, i.e. 1613 K, of the CrMnFeCoNi alloy [29]. Therefore, the whole melt pool, i.e. inside the purple outline, was visible. The temperature reached a peak value, approximately in the melt pool center, and decreased with the distance from the melt pool center. Temperature data were extracted and are plotted along the white dashed line, i.e. along the laser scan direction and through the hottest (peak temperature) point in the melt pool, as shown in Fig. 3 (b). The zero value on the X axis indicated the hottest point. The temperature curve was divided, using the hottest point, into two parts, with these two parts experiencing the heating and cooling processes, respectively. We paid more attention to the cooling part in this study. The liquidus temperature T_L of the equiatomic CrMnFeCoNi alloy was indicated by the horizontal dashed line in Fig. 3 (b), and the crossover point between the cooling part and the liquidus temperature was the boundary between the liquids and the mushy zone, i.e. the region where liquids and solids co-existed, and solidification was occurring. The solidification conditions in the vicinity of this crossover point are important for as-solidified microstructure formation and were investigated in this study.

From the cooling part of the temperature curve, the temperature gradient and cooling rate curves were calculated accordingly and are plotted in Fig. 3 (c) and (d),

respectively. The temperature gradient curve was obtained by differentiating the temperature curve with distance, and the cooling rate curve was obtained by multiplying the temperature gradient by the laser scan speed, i.e. 5 mm/s. The temperature gradient and cooling rate curves exhibited the same trends, both of which decreased initially and then increased with the distance from the hottest point. The temperature gradient, $G_{liquidus}$, and cooling rate, $CR_{liquidus}$, values at the crossover point were calculated to be 347 K/mm and 1732 K/s, respectively.

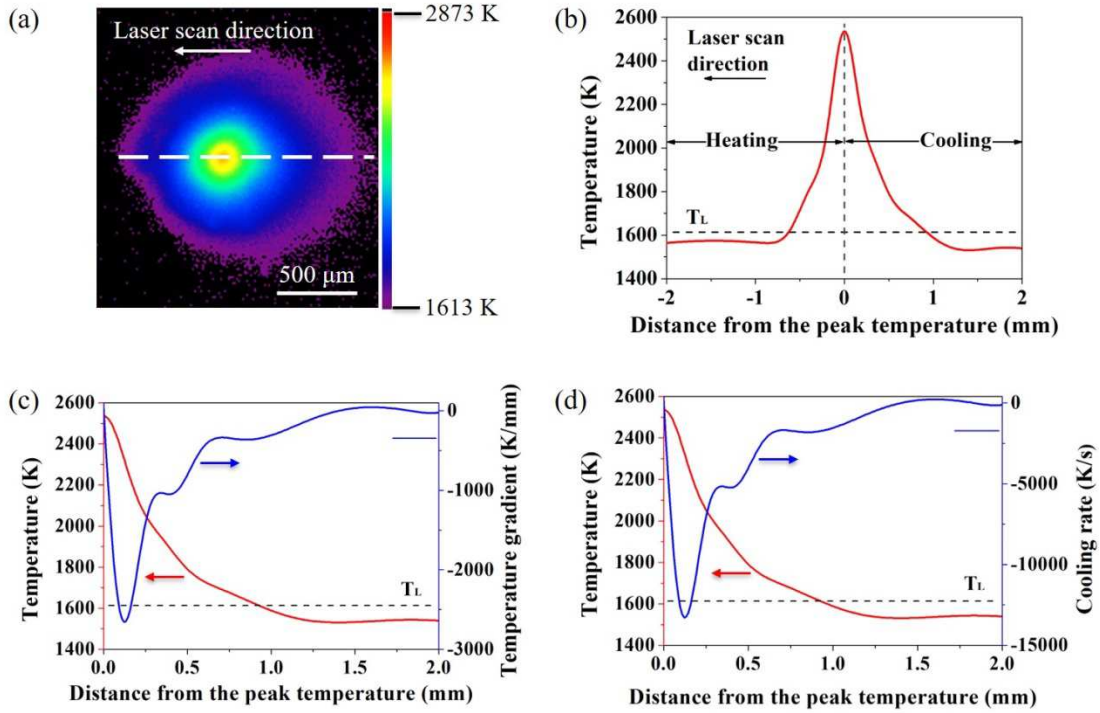

Fig. 3. (a) A typical colorized thermal map of the melt pool looking from the top; (b) Temperature curve which was along the laser scan direction and through the hottest point in the thermal map in (a); (c) Temperature (red line) and temperature gradient (blue line) curves; (d) Temperature (red line) and cooling rate (blue line) curves. The liquidus temperature T_L=1613 K is indicated by the black broken line in (b)-(d).

3.3. Phase formation

Fig. 4 (a) shows the XRD pattern of the LENS^{TM}-deposited CrMnFeCoNi

specimen, with the XY-plane examined. Only a single disordered face centered cubic (FCC) structured phase was detected, which is in good agreement with its counterparts manufactured by conventional metallurgical routes [9, 10, 30] and alternative AM processes [11]. The single-phase characteristic was rationalized by the solidification path simulated by Scheil's model with the aid of the high entropy alloys database, as shown in Fig. 4 (b). According to the simulated solidification path, only a single FCC phase solidified from the liquid, i.e. L→L+FCC→FCC. It should be noted that, at lower temperatures, the single-phase structure has been proven to be thermodynamically unstable, and multiple precipitates may be formed in the matrix [31-33]. However, a very long annealing time was a prerequisite to establish the thermodynamic equilibria and lead to the precipitate formation, which could not be fulfilled in the present case. Therefore, the single-phase disordered solid solution structure in the just solidified state was retained down to room temperature. Furthermore, we observed that the predicted liquidus temperature (i.e. 1596 K) by Scheil's model was in good agreement with the measured value of 1613 K [29].

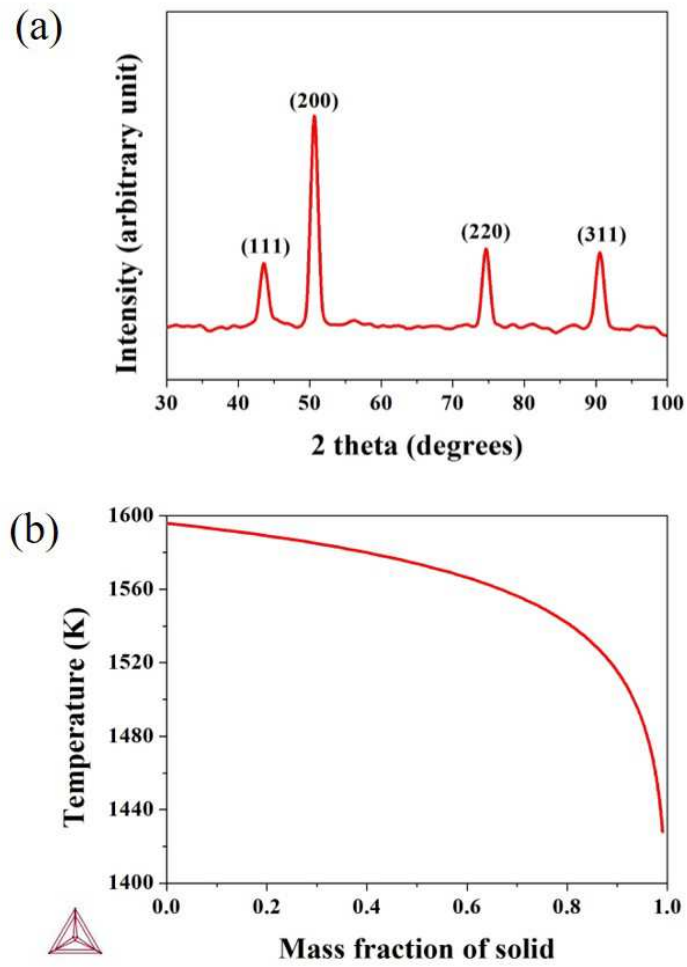

Fig. 4. (a) XRD pattern of the LENS^{TM}-deposited CrMnFeCoNi specimen, with the XY-plane examined; (b) Solidification path (L→L+FCC→FCC) of the CrMnFeCoNi alloy calculated by Scheil's model with the aid of the high entropy alloys database. Both results confirm the single-phase disordered FCC structure of the LENS^{TM}-deposited CrMnFeCoNi alloy.

3.4. As-deposited microstructures

Fig. 5 shows the longitudinal cross-sectional, i.e. the XZ plane, microstructures of the CrMnFeCoNi alloy in the as-deposited state. The layer-by-layer deposition patterns are visible, with the melt pool boundaries and layer boundaries indicated, as shown in Fig. 5 (a). The average layer thickness was determined to be 154 μm based

on optical micrographs. The deposition patterns are closely related to the laser scan strategy [34-37]. For the bidirectional and cross-hatched scan strategy used in the present study, the as-deposited specimen exhibits a periodic deposition pattern with a cycle of two layers, i.e. the layers 1, 3, and 5 correspond to the laser scan along the X direction, and the layers 2, 4 and 6 correspond to the laser scan along the Y direction. The distance between two adjacent melt pool bottoms corresponds to a hatch spacing of 460 μm. The enlarged optical micrograph shows that the melt pool solidification was dominated by columnar growth, approximately along the maximum heat flux direction that was perpendicular to the melt pool boundaries (Fig. 5 (b)). As the LENS^{TM}-deposited CrMnFeCoNi alloy exhibited a single-phase FCC solid solution structure (Fig. 4), each columnar grain could be seen as a tiny FCC-structured single crystal. Fig. 5 (c) and (d) give the inverse pole figure (IPF) and kernel average misorientation (KAM) maps of a same region of 900 μm by 900 μm, respectively. The grains in the IPF map were colorized based on their orientations with respect to the building direction (i.e. the Z axis). The high angle grain boundaries (HAGBs, misorientation > 15°) were highlighted in black in the IPF and KAM maps, and based on the HAGBs, the average grain size (i.e. the average width) of the columnar grains was estimated to be 13 μm. Furthermore, a large color variation was observed within the individual grains (Fig. 5 (c)), indicating the large local misorientation across the grains. This was further evidenced in the KAM map. As for the large local misorientation within the grains, we attribute it to the solidification substructures and high dislocation densities in the as-deposited specimen, as revealed by the ECCI images in Fig. 6. It can be seen from Fig. 6 (a) that within columnar grains some micron sized (2 ~ 5 μm) solidification substructures were formed as indicated by the white arrows. These substructures were either cellular or pillar shaped, which were

view-angle-dependent. High densities of dislocations (i.e. the white lines) were observed within these substructures, as shown in Fig. 6 (b) and (c). It should be mentioned that the residual stress in the LENS^{TM}-deposited CrMnFeCoNi alloy was measured to be approximately 182 MPa (the average value of residual stresses measured at three points). The existence of residual stress indicates the plastic deformation inside the specimen, which coincides with the observed high density of dislocations. These dense dislocations are deemed associated with the mechanical behavior in a specific way and are discussed in *Section 4.2*.

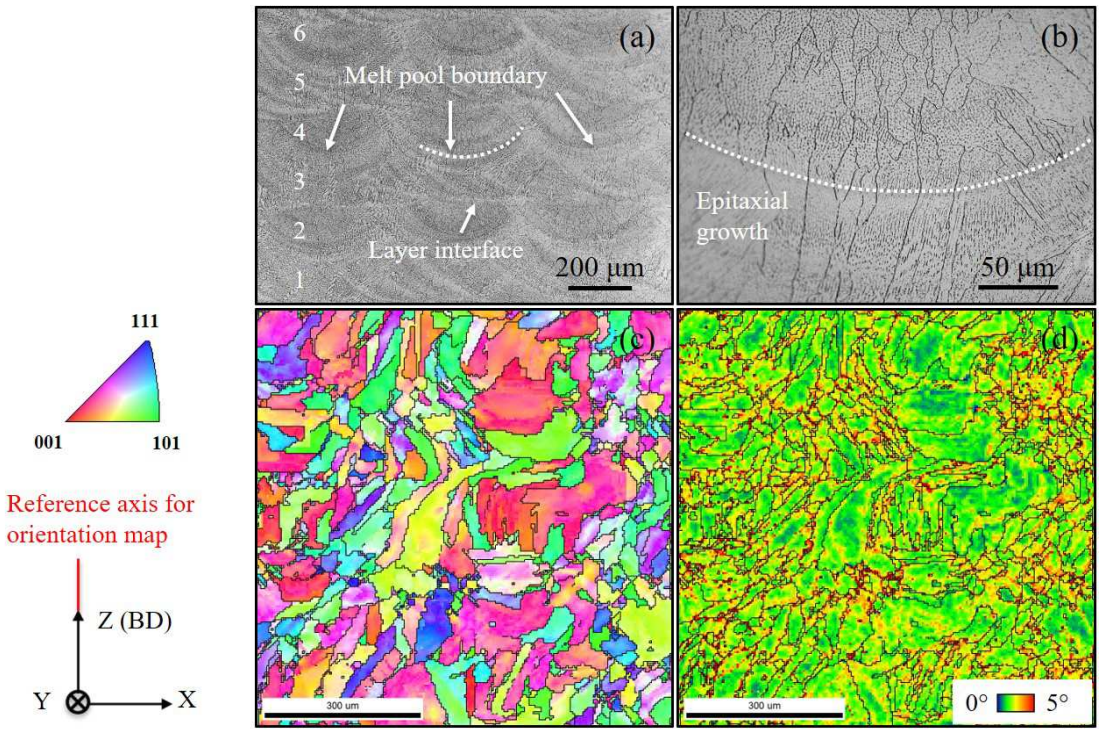

Fig. 5. The longitudinal cross-sectional (i.e. the XZ plane) microstructures of the CrMnFeCoNi alloy in the as-deposited state. (a) and (b) Optical micrographs showing the layer-by-layer deposition patterns and the epitaxial growth mode, respectively; (c) and (d) IPF and KAM maps of a region of 900 μm by 900 μm, respectively. The high angle grain boundaries (HAGBs, misorientation > 15°) were highlighted in black in (c) and (d). The reference axis for the IPF map is the building direction.

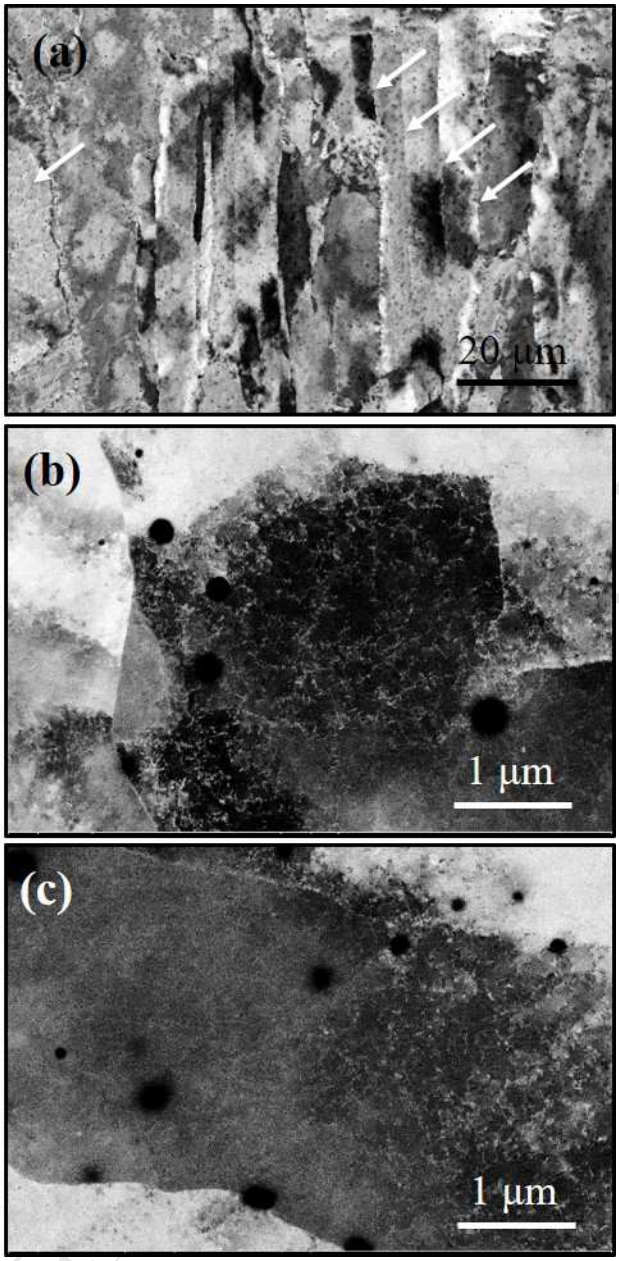

Fig. 6. ECCI images of the LENS^{TM}-deposited CrMnFeCoNi alloy showing (a) solidification substructures and (b-c) high dislocation densities. Some solidification substructure boundaries are indicated by the white arrows in (a). The dislocations in (b) and (c) appear bright as compared with the matrix under the current diffraction conditions.

Fig. 7 (a) gives the elemental distribution in a region containing several solidification substructures. It can be seen that Mn and Ni segregated at the substructure walls, and Co, Cr, and Fe segregated in the substructure interiors. The

elemental concentration in the remaining liquid as a function of the temperature was simulated by Scheil's model with the aid of the high entropy alloys database, and is shown in Fig. 7 (b). It can be seen that with the decrease of the temperature, the concentrations of Mn and Ni in the remaining liquid increased, and the concentrations of Fe, Cr, and Co showed the opposite trend. Based on the simulated results, the solidification process of the CrMnFeCoNi alloy can be regarded as a process of rejecting Mn and Ni atoms into the remaining liquid, leading to the enrichment of Fe, Cr, and Co atoms in the first solidified regions, i.e. substructure interiors, and the enrichment of Mn and Ni atoms in the later solidified regions, i.e. substructure walls. Clearly, the simulated and experimental results agree well with each other.

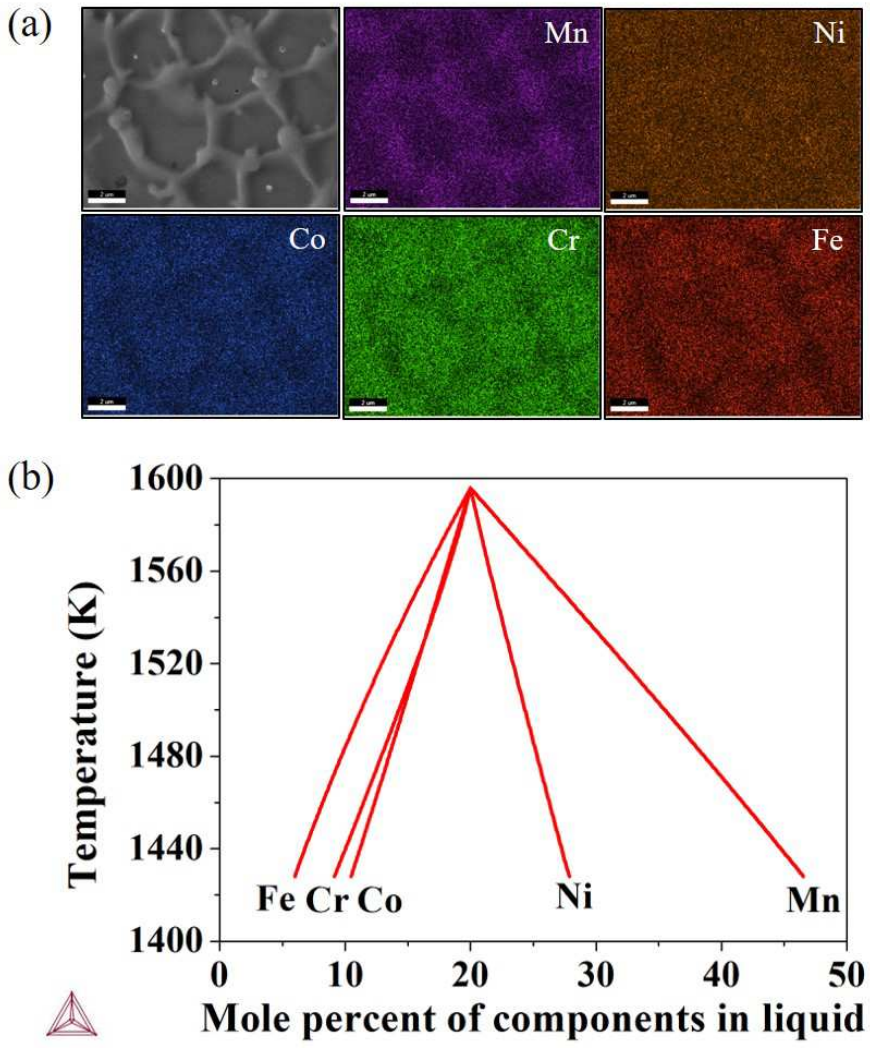

Fig. 7. Elemental micro-segregation of the CrMnFeCoNi alloy during solidification. (a) EDS elemental mapping of a region of several solidification substructures; (b) Compositional evolution of the remaining liquid simulated by Scheil's model with the aid of the high entropy alloys database. All scale bars in (a) are 2 μm. Both elemental mapping and simulated compositional evolution show the segregation of Co, Cr and Fe at first solidified regions (i.e. solidification substructure interiors), and the segregation of Mn and Ni at later solidified regions (i.e. solidification substructure walls) during solidification.

3.5. Tensile behavior

The typical engineering tensile stress-strain curve at ambient temperature of the LENS^{TM}-deposited CrMnFeCoNi alloy is shown in Fig. 8 (a). The engineering yield strength, i.e. the stress at which 0.2% plastic deformation occurs, σ_y, and the strain to failure, ε_f, were measured to be 517 MPa and 26%, respectively. Furthermore, uniform tensile elongation was measured to be 17% which is the engineering strain value corresponding to the maximum point, i.e. the ultimate tensile stress, on the engineering stress-strain curve. When the maximum point was reached, nonuniform plastic deformation begins, and geometric instability, i.e. necking phenomenon, occurs. Clearly, the uniform tensile elongation is an important measure of the ductility of an alloy. Fig. 8 (b) gives the typical SEM secondary electron image of the tensile fracture surface. The ductile fracture characteristic can be confirmed from a vast number of fine dimples on the fracture surface.

Fig. 9 shows the microstructure of the LENS^{TM}-deposited CrMnFeCoNi alloy that was tensile tested to fracture. The deformed microstructures investigated both by EBSD and by ECCI were approximately 3 mm far from the fracture surface to avoid

the necking region, and therefore the investigated regions experienced uniform plastic deformation during the tensile test. Twins were occasionally observed in the IPF map and further confirmed by the misorientation profile, as shown in Fig. 9 (a) and (b). Due to the absence of twins of any types, i.e. growth, annealing, or deformation/mechanical, prior to straining, these twins are formed during the tensile process and are classified as deformation twins. Fig. 9 (c) and (d) give the ECCI images of these deformation twins at different magnifications. It can be seen that the thickness of these deformation twins was about 50 nm. It is also noted that the step size 1 μm for EBSD characterization is larger than the nanotwin thickness, and therefore the nanotwins seem not continuous and intact in the IPF map (Fig. 9 (a)). However, since the electron beam size is far below 50 nm, the crystallographic information could still be obtained when the beam hits the twin region, and thus the combination of the misorientation profile in Fig. 9 (b) and the ECCI investigations in Fig. 9 (c) and (d) can confirm the twin relationship. In view of the slight degree of the twinning, the deformation process is reckoned to be dominated by dislocation activities which are shown in Fig. 9 (e). The deformation mechanisms and their contributions to the uniform tensile ductility are discussed in detail in *Section 4.3*.

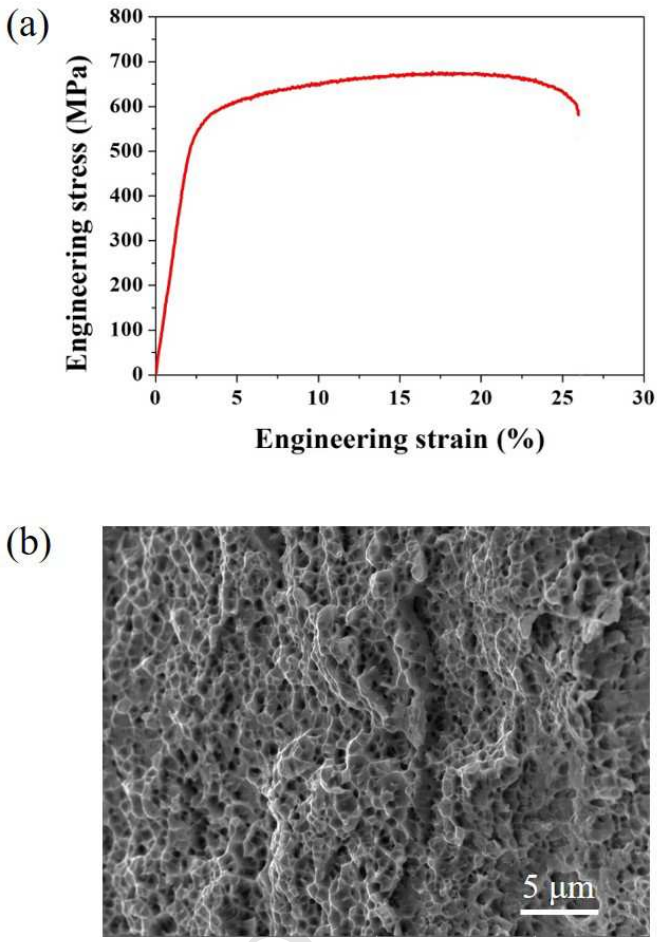

Fig. 8. Tensile behavior of the LENS^{TM}-deposited CrMnFeCoNi specimen at room temperature. (a) Engineering stress-strain curve; (b) Fracture surface.

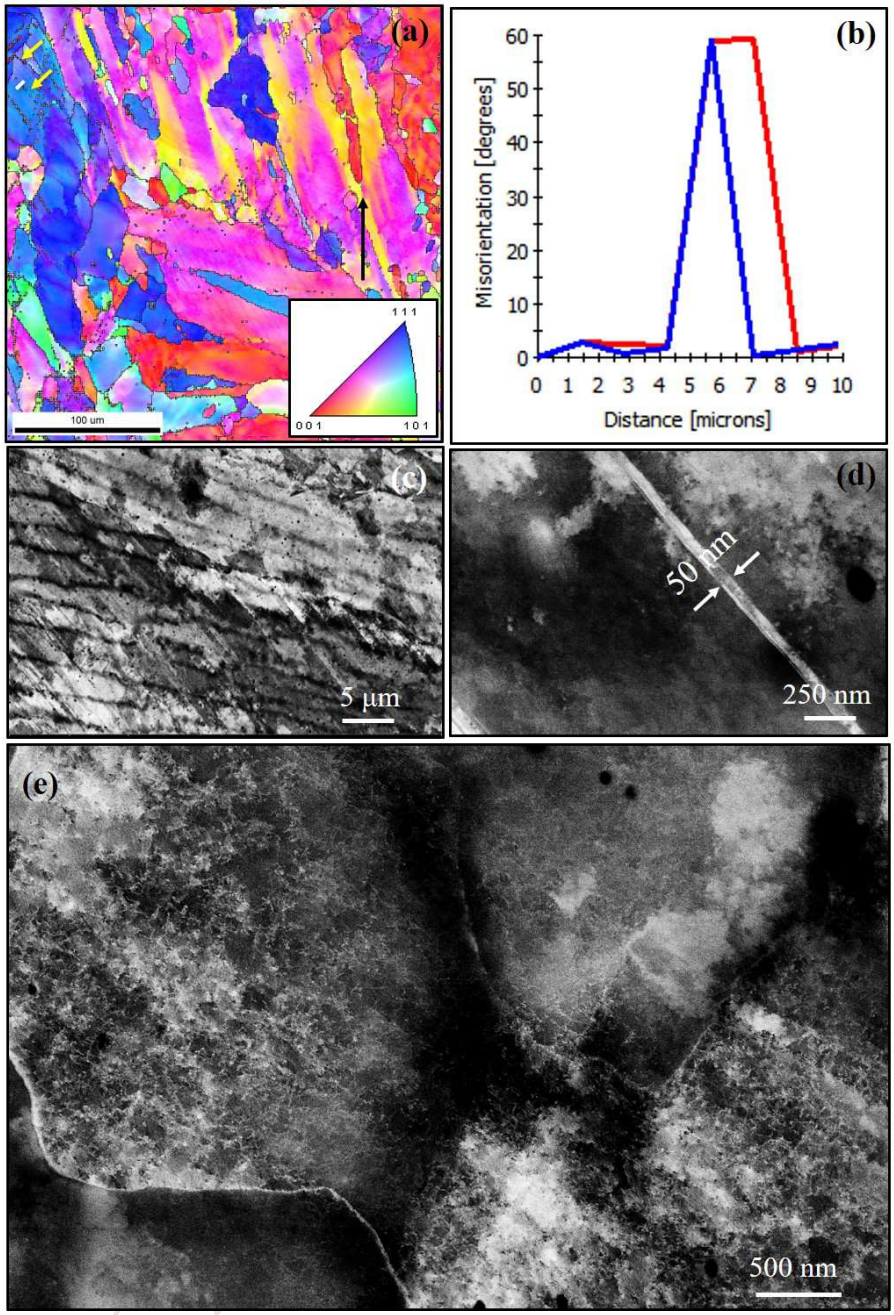

Fig. 9. Microstructures of the LENS^{TM}-processed CrMnFeCoNi alloy tensile tested to fracture. (a) EBSD IPF map with the reference axis (black arrow) aligned vertically upwards. Deformation twins are indicated by the yellow arrows; (b) Misorientation profile plotted over the white solid line in the IPF map (red line: point-to-point; blue line: point-to-origin); (c) and (d) ECCI images at different magnifications showing nanoscale deformation twins; (e) ECCI image showing the dislocation substructures in the deformed microstructure.

4. Discussion

4.1. Formation of the as-deposited microstructures

The as-deposited microstructures at multiple length scales, i.e. columnar grains, solidification substructures, and dislocation substructures, are formed. Clearly, the columnar growth, rather than the equiaxed growth, dominates the melt pool solidification of the CrMnFeCoNi alloy. This is consistent with the AM-processed conventional alloys, such as Ni-based superalloys [35] and titanium alloys [38], and is mainly attributed to the intrinsically high thermal gradient, i.e. 347 K/mm in the present study. Furthermore, the average grain size (13 μm) in the LENS^{TM}-deposited CrMnFeCoNi alloy is much finer than that reported for CrMnFeCoNi alloys (100-300 μm grain size [11, 25]) processed by other powder-blown AM processes. This is largely due to two reasons. First, the linear heat input used in the present study is much lower than that reported in the literature (80 J/mm in this work vs 120 ~ 850 J/mm in Refs. [11, 25]). The lower linear heat input normally results in a higher cooling rate, which facilitates the formation of finer microstructures. Furthermore, the grain size and the crystallographic orientation of the substrate are also believed to play an important role in grain growth and selection during solidification, and hence the final grain size [39]. However, this is not discussed in the present paper due to insufficient microstructural details of the substrate. In addition, a very high density of dislocations is formed in the LENS^{TM}-deposited CrMnFeCoNi alloy, which is also reported for the AM-processed 316L stainless steel [40-42], and Inconel 718 superalloy [43]. The formation of such dense dislocations is possibly due to the development of the internal stress, and hence the internal strain, as the parts rapidly cool down to the ambient temperature after solidification. The gradually accumulated

thermal strain in the AM-processed parts has to be accommodated, at least partially, by the dislocations. The effect of the accumulated dislocations on the yield strength is discussed in *Section 4.2*. Finally, elemental segregation at the micrometer scale is observed, with the cellular interior enriched in Co, Cr and Fe, and the cellular wall enriched in Mn and Ni. This is consistent with the observed dendritic segregation in the as-cast counterparts despite different solidification substructures, i.e. celluar for LENS^{TM}, and dendritic for casting [29, 44, 45].

4.2. Strengthening mechanisms

4.2.1. The yield strength of the LENS^{TM}-deposited CrMnFeCoNi alloy

The yield strength of a polycrystalline alloy is known to be the critical applied stress which can activate the dislocation motion in the vast majority of the grains and thus lead to the onset of the macro plastic deformation. This critical applied stress value (i.e. the yield strength) is determined by the microstructural features, i.e. base-metal lattice, interstitial or substitutional solute atoms, nanotwins, precipitates, grain boundaries, and initial dislocations. As the LENS^{TM}-deposited CrMnFeCoNi alloy is nanotwin-free, the contribution from the nanotwins can be disregarded. It should be noted, however, that the nano-twinning behavior after yielding point was observed in this study (Fig. 9), but it does not contribute to the yield strength but to the work hardening, and is discussed in *Section 4.3.3*. Furthermore,, the precipitation phases have been found in many alloys, such as Ni-based alloys and steels, and several models (e.g. Friedel's shear cutting model [46], and Mohles' dislocation dynamics model [47]) have been proposed to evaluate its contribution to the overall yield strength. However, as indicated by the XRD pattern and calculated solidification path (Fig. 4), the LENS^{TM}-deposited CrMnFeCoNi alloy exhibits a single-phase FCC

structure, and therefore the precipitation hardening mechanism doesn't operate in this alloy, and its corresponding contribution can be also disregarded.

As for the solute atoms, they are normally discussed in dilute solid solution alloys with a single base metal, i.e. the solvent lattice, plus a certain amount of interstitial and substitutional solute atoms. These interstitial or substitutional solute atoms generate a local stress field which hinders the dislocation motion and therefore strengthen the alloy. However, in the present case, the CrMnFeCoNi alloy is a concentrated solid solution system with five elements in equiatomic ratios. All these five elements occupy the FCC lattice randomly, and no distinct solvent lattice and solute atoms exist. Therefore, for the CrMnFeCoNi alloy, the resistance from the solute atoms which is normally discussed in conventional alloys has to be converted to the lattice friction stress. Based on the above analysis, the yield strength of the LENS^{TM}-deposited CrMnFeCoNi alloy can be predicted by adding the contributions from the base-metal lattice friction, grain boundaries, and initial dislocations:

$$\sigma_{\mathrm{y}} = \sigma_{\mathrm{o}} + \Delta\sigma_{\mathrm{GBS}} + \Delta\sigma_{\mathrm{DS}} \quad (1)$$

where σ_{o}, $\Delta\sigma_{\mathrm{GBS}}$, and $\Delta\sigma_{\mathrm{DS}}$ represents yield stresses resulting from the lattice friction, grain boundary strengthening, and dislocation strengthening, respectively. But as discussed earlier, the σ_{o} value here is the resistance from a complex lattice of all these five constituent atoms rather than from the base metal. The σ_{o} value of the CrMnFeCoNi alloy at 293 K has been experimentally determined to be 125 MPa, in Ref. [9] and 194 MPa, in Ref. [48], respectively. In this study, their average value of 160 MPa is adopted. In the following, the contributions from grain boundary strengthening and dislocation strengthening are assessed based on classical equations and microstructural details achieved experimentally in *Section 3*.

Grain boundary strengthening mechanism operates in all polycrystalline alloys, and the grain refinement introduces higher concentrations of incoherent grain boundaries which more strongly block the dislocation motion and therefore strengthen the alloy. For microcrystalline alloys, the yield stress resulting from the grain boundary strengthening effect, $\Delta\sigma_{GBS}$, can be estimated by [9]:

$$\Delta\sigma_{\mathrm{GBS}} = k \cdot d^{-0.5} \tag{2}$$

where k=494 MPa·μm$^{0.5}$ is the Hall-Petch coefficient for slipping at 293 K [9], and d is the average grain size. The $\Delta\sigma_{GBS}$ value is calculated to be 137 MPa for the grain size of 13 μm in this study. In addition to the grain boundary strengthening effect, the high density of initial dislocations in the AM-ed alloys is also frequently regarded as an effective strengthening mechanism [24, 49]. The yield stress resulting from the dislocation strengthening effect, $\Delta\sigma_{DS}$, can be estimated according to the Taylor hardening law [50]:

$$\Delta\sigma_{\mathrm{DS}} = M\alpha Gb\sqrt{\rho} \tag{3}$$

where the Taylor factor M was estimated to be 3.06 [51], α=0.2 is a constant for FCC structured alloys, the shear modulus G was measured to be 80 GPa at 293 K [52, 53], b is the magnitude of the Burgers vector (<110>/2) of the full dislocation and was determined to be 0.2539 nm [54], and ρ is the initial dislocation density, i.e. the total length of dislocations per unit volume of the material. As indicated by Eq. (3), increasing the dislocation density, ρ, increases the $\Delta\sigma_{DS}$ value, due to the stronger interactions between the stress fields of dislocations. As shown in Fig. 6, the CrMnFeCoNi alloy in the as-deposited state exhibits a high density of dislocations, and the dislocation density, ρ, can be roughly estimated by following equations [55,

56]:

$$\rho = 2\sqrt{3}\varepsilon/(Db) \quad (4)$$

$$\beta cos\theta = K\lambda/D + 4\varepsilon sin\theta \quad (5)$$

where ε is the micro-strain, D is the crystallite size, b is again the magnitude of the Burgers vector (<110>/2) of the full dislocation, β is the full width at half maximum (FWHM) of the analyzed peaks from the XRD profile after subtracting the instrumental line broadening, θ is the Bragg angle of the analyzed peaks, K is a dimensionless shape factor with a value of 0.89, and λ is the X-ray wavelength that equals to 0.154056 nm for Cu-K_α radiation.

Based on Eqs. (4) and (5), the dislocation density ρ in the LENS^{TM}-deposited CrMnFeCoNi alloy is estimated to be 3×10^{14} m^{-2}. Putting the estimated ρ value into Eq. (3), the yield stress resulting from the initial dislocations is estimated to be 215 MPa. The calculated yield strength (i.e. $\sigma_o+\Delta\sigma_{GBS}+\Delta\sigma_{DS}$=512 MPa) resulting from the lattice friction resistance, fine-grain strengthening effect, and dislocation strengthening effect agrees well with the measured value of 517 MPa. It also indicates that the yield strength of the LENS^{TM}-deposited CrMnFeCoNi alloy originates from multiple strengthening mechanisms, especially the dislocation strengthening mechanism whose contribution accounts for ~ 42% of the total yield strength. In other words, the highly dense dislocations of the LENS^{TM}-deposited CrMnFeCoNi alloy contribute to its yield strength significantly.

4.2.2. Compared with conventionally manufactured CrMnFeCoNi alloys

Section 4.2.1 discusses the yield strength of the LENS^{TM}-deposited

CrMnFeCoNi alloy based on classical equations (i.e. Hall-Petch relationship, and Taylor hardening law) and experimentally achieved microstructural details (i.e. grain size and dislocation density). The variation of microstructural details, which can be achieved by changing the processing route, affects a lot the yield strength of an alloy. Fig. 10 shows a summary of the tensile yield strength versus uniform tensile elongation of the CrMnFeCoNi alloy manufactured by various routes. These include casting [11, 44], cold deformation, i.e. cold forging and rolling, followed by annealing [9, 10, 48], high pressure torsion followed by post-deformation annealing (HPT+PDA) [15], mechanical alloying followed by spark plasma sintering (MA+SPS) [14], selective laser melting (SLM) [22-24], and various laser powder-blown AM processes (i.e. laser metal deposition (LMD) [11], laser additive manufacturing (LAM) [25, 26], laser aided additive manufacturing (LAAM) [27], laser 3D printing [28], and LENS^{TM}, i.e. the present work). It should be noted that different universities, labs or companies may use different terminologies to denominate the laser powder-blown AM process, however, they all build a part by remelting the surface of previous layers and simultaneously feeding metal powders into the remelted region, i.e. melt pool. Therefore, these processes can be classified into the same type in essence (i.e. using the laser as the heat source, and feeding powders by nozzles), and therefore in Fig. 10 we unify them as laser powder-blown AM process. These CrMnFeCoNi alloys are grouped into three categories, i.e. coarse-grained (CG, up to hundreds of micrometers), fine-grained (FG, 500 nm to a dozen or so micrometers), and ultrafine-grained or even nanocrystalline (UFG, < 500 nm; NC, < 100 nm), depending upon their grain sizes. It can be seen from Fig. 10 that the yield strength of the CrMnFeCoNi alloy approximately ranges from 170 to 1600 MPa, depending on the processing route and the resultant microstructure.

For the as-casted CrMnFeCoNi alloy, besides the lattice friction stress, only the grain boundary strengthening mechanism contributes to its yield strength. And considering its coarse grains, the yield strength of the as-casted CrMnFeCoNi alloy is extremely low based on Eq. (2). Until now, most of the CrMnFeCoNi alloys are fabricated by cold deformation followed by annealing, and this specific kind of the CrMnFeCoNi alloy is referred to as wrought-annealed CrMnFeCoNi alloy in this study. For the wrought-annealed CrMnFeCoNi alloy, the grain boundary strengthening mechanism also operates, and its contribution to the yield strength is determined by the grain size. As reported in published works [9, 10, 48], the grain size of the wrought-annealed CrMnFeCoNi alloy may range from 155 to 0.5 μm, and the yield stress resulting from the grain boundary strengthening mechanism is therefore calculated to be from 40 to 865 MPa based on Eq. (2), i.e. $\Delta\sigma_{GBS}=40\sim865$ MPa. Furthermore, as the high dislocation density introduced during cold deformation is dramatically decreased during the recrystallization annealing treatment, the dislocation density is extremely low in the as-annealed state [8, 9]. The dislocation density in the as-annealed alloy is normally of the order of $10^{11}\sim10^{12}$ m^{-2} [57]. Even when adopting the upper limit of 10^{12} m^{-2}, the calculated $\Delta\sigma_{DS}$ is only 12 MPa, which is much lower than that of the LENS^{TM}-deposited CrMnFeCoNi alloy. The total yield stress of the wrought-annealed CrMnFeCoNi alloy resulting from all possible strengthening mechanisms is therefore calculated to be 212 to 1037 MPa, i.e. $\sigma_0+\Delta\sigma_{GBS}+\Delta\sigma_{DS}=212\sim1037$ MPa, which well agrees with the experimental values (Fig. 10). For the CrMnFeCoNi alloys fabricated by HPT+PDA or MA+SPS processes [14, 15], the grain size can be further reduced and even fallen into UFG and NC regimes. For this case, the dependence of the yield stress resulting from the grain boundary

strengthening mechanism on the grain size cannot be precisely predicted by Eq. (2) that well applies to the microcrystalline alloys. But the strengthening effect is almost continuously observed when reducing grain sizes down to ~10 nm, and the yield strength of such UFG/NC CrMnFeCoNi alloys reaches above ~1000 MPa. Despite of the excellent yield strength, their uniform tensile elongation is very low. Overall speaking, a relatively good combination of the tensile yield strength and uniform tensile elongation is achieved in the FG regime. Fortunately, the LENS^{TM}-deposited CrMnFeCoNi alloy in this work also exhibits a FG microstructure, i.e. 13 μm grain size, and this is largely attributed to the rapid cooling rate, i.e. 1732 K/s, during melt pool solidification. Furthermore, it can be clearly seen that the high initial dislocation density activates an additional strengthening mechanism, i.e. dislocation strengthening, and therefore endows the LENS^{TM}-deposited CrMnFeCoNi alloy with a higher tensile yield strength than the wrought-annealed FG counterparts with similar grain sizes. By contrast, however, the uniform tensile elongation is lowered, which is discussed in *Section 4.3*.

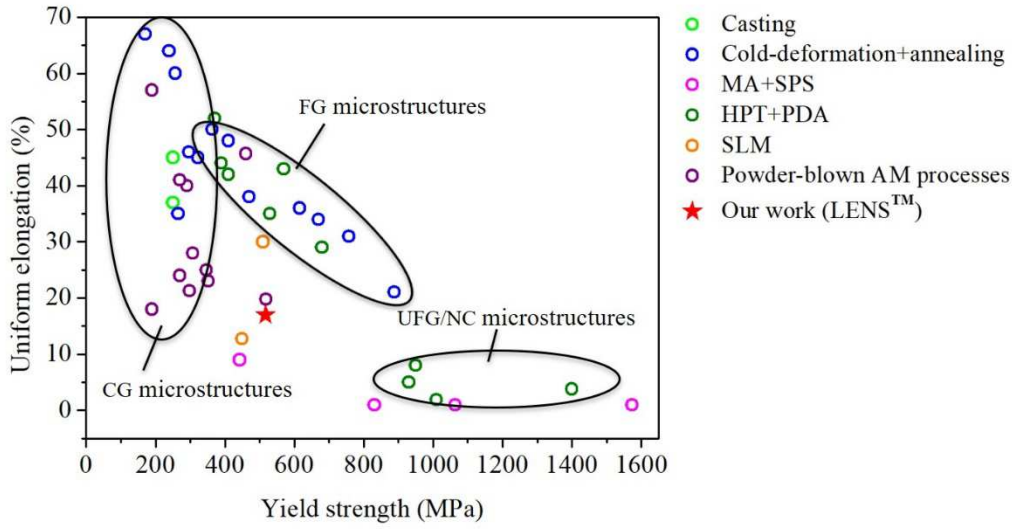

Fig. 10. A summary of tensile yield strength versus uniform tensile elongation for

CrMnFeCoNi alloys manufactured via various routes, including casting [11, 44], cold deformation, i.e. cold forging and rolling, followed by annealing [9, 10, 48], high pressure torsion followed by post-deformation annealing (HPT+PDA) [15], mechanical alloying followed by spark plasma sintering (MA+SPS) [14], selective laser melting (SLM) [22-24], and various laser powder-blown AM processes [11, 25-28], and LENS^{TM}, i.e. the present work). From a microstructural perspective, these alloys are classified into CG, FG, UFG/NC CrMnFeCoNi alloys.

4.3. Origin of reduced ductility

4.3.1. Evaluation of work hardening capability

As analyzed in *Section 4.2*, the yield strength of the LENS^{TM}-deposited CrMnFeCoNi alloy compares favorably with its wrought-annealed counterparts with similar grain sizes. However, its uniform tensile elongation is lowered, as can be seen from Fig. 10. Actually, reduced ductility is also commonly reported for the laser-based additively manufactured conventional alloys, e.g. 316L stainless steel [58], and titanium alloys [59, 60]. However, this phenomenon is not well understood to date. In this study, we compare the work hardening capabilities of the LENS^{TM}-deposited and wrought-annealed CrMnFeCoNi alloys. Fig. 11 shows the true stress versus logarithmic strain curves that are calculated from the engineering ones, and the plots of the true work hardening rate (WHR, h), i.e. the derivative of the true stress with respect to the logarithmic strain, as a function of the logarithmic strain. The data for the wrought-annealed CrMnFeCoNi alloy (17 μm grain size) is extracted from Ref. [8]. It can be seen from Fig. 11 that the WHR values are initially high but decrease with the logarithmic strain for both alloys. However, the WHR value of the LENS^{TM}-deposited CrMnFeCoNi alloy, by contrast, drops more rapidly during

straining. This leads to the earlier intersection of the WHR- and true stress-logarithmic strain curves at a lower strain level. The crossover point indicates that the WHR value equals to the true stress, and at this critical point, the strain localization, i.e. the necking phenomenon, occurs according to the Considère's criterion [61]. In other words, the relatively inadequate work hardening capability of the LENS^{TM}-deposited CrMnFeCoNi alloy leads to its earlier necking and hence reduced uniform tensile elongation, i.e. 17% of the LENS^{TM}-deposited CrMnFeCoNi alloy vs ~ 35% of the wrought-annealed counterpart.

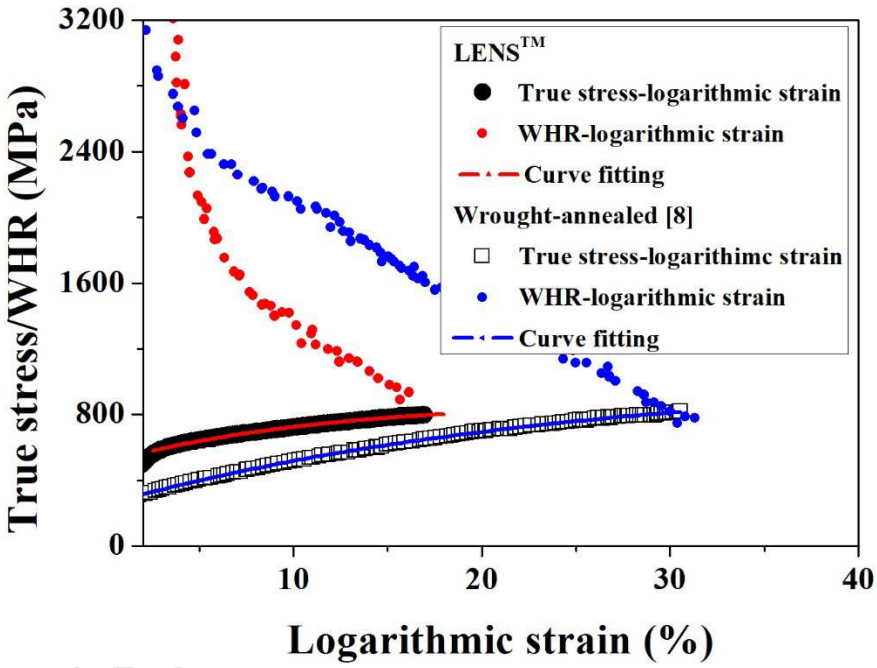

Fig. 11. Measured true stress-logarithmic strain curves, work hardening rate (WHR) curves, and curve fitting results for the LENS^{TM}-deposited and wrought-annealed CrMnFeCoNi alloys. The measured true stress-logarithmic strain curve and the WHR curve for the wrought-annealed CrMnFeCoNi alloy is abstracted from Ref. [8]. The true stress-logarithmic strain data for both alloys are fitted by Eq. (12).

4.3.2. Origin of work hardening

The mechanisms underlying the relatively inadequate work hardening capability needs to be clarified in terms of the evolution of the deformation substructures, i.e. the dislocation and nanotwin substructures, during straining. These deformation substructures can act as efficient barriers to hinder the gliding dislocations and therefore harden the alloys. In other words, the evolution of these deformation substructures governs the work hardening capability. As reported by Laplanche et al. [8], the dislocation density of the wrought-annealed CrMnFeCoNi alloy increases dramatically during straining, and these dislocations tend to tangle or even form dislocation cells (DCs) to minimize the elastic energy per unit length of the dislocation line. Such highly dense dislocation substructures effectively block the dislocation motion and therefore contribute to the work hardening capability. In addition to the dislocation multiplication, nanoscale deformation twins are reported to form after ~20% logarithmic strain, corresponding to ~720 MPa true stress [8]. As deformation progresses further, the volume of the deformation twins increases and the twin spacing decreases. As is well known, the arrangements of atoms on both sides of the twin boundaries are mirror reflections, and the formation of the twin boundaries leads to a continuous grain refinement process and thus a reduction in the mean free path of the dislocations, i.e. the dynamic Hall-Petch effect [62]. The combined effects of the dislocation multiplication and nanoscale deformation twinning lead to the substantial work hardening capability and thus the significant uniform tensile ductility of the wrought-annealed CrMnFeCoNi alloy.

4.3.3. The onset of twinning

As for the twining behavior, it is not always observed during the tensile test of the wrought-annealed CrMnFeCoNi alloy. For instance, deformation twins are not

observed in the FG (503 nm grain size, which nearly falls into the UFG regime) wrought-annealed CrMnFeCoNi alloy which has been strained to failure at a logarithmic strain of nearly 30% [48]. Fortunately, the desirable twinning behavior is observed during the straining process of our LENS^{TM}-deposited CrMnFeCoNi alloy. To determine the onset of the deformation twins, the twinning stress, i.e. the critical true stress beyond which the twinning behavior is activated, is estimated in this study. The twinning stress has been found to be grain size dependent in conventional alloys [63-66], and a Hall-Petch type relationship is normally followed [63]:

$$\sigma_{\mathrm{tw}} = \sigma_{\mathrm{tw,o}} + k_{\mathrm{tw}} \cdot d^{-0.5} \tag{6}$$

where σ_{tw} is the twinning stress, $\sigma_{\mathrm{tw,o}}$ is the twinning stress for a single crystal, k_{tw} is the Hall-Petch coefficient for twinning, and d is again the average grain size. The $\sigma_{\mathrm{tw,o}}$ value can be estimated by [66]:

$$\sigma_{\mathrm{tw,o}} = M\gamma_{\mathrm{SF}}/b_{\mathrm{s}} \tag{7}$$

where M is again the Taylor factor, γ_{SF} is the stacking fault energy (SFE) that was determined to be 18 ~ 27 mJ/m^2 for the CrMnFeCoNi alloy [67, 68], b_{s}=0.1466 nm [54] is the magnitude of the Burgers vector (<112>/6) of the Shockley partial dislocation. Combining Eqs. (6) and (7), we get:

$$\sigma_{\mathrm{tw}} = M\gamma_{\mathrm{SF}}/b_{\mathrm{s}} + k_{\mathrm{tw}} \cdot d^{-0.5} \tag{8}$$

Eq. (8) indicates that the twinning stress σ_{tw} increases with the decrease in the grain size d. Assuming the twinning stress σ_{tw}=720 MPa for a grain size d=17 μm [8], the Hall-Petch coefficient for twinning, k_{tw}, is determined to be 1164 MPa·μm$^{0.5}$ that

is more than two times higher than the Hall-Petch coefficient for slipping, i.e. 494 $MPa \cdot \mu m^{0.5}$. This trend is consistent with previous studies that report the ratio of the Hall-Petch coefficient for twinning to that for slipping ranges from 1 ~ 4 for FCC-structured alloys [63, 69]. The much larger Hall-Petch coefficient for twinning indicates that the twinning stress is more strongly grain size dependent as compared with the grain size dependency of the yield strength. The twinning stress for the CrMnFeCoNi alloy with grain sizes of 13 and 0.503 μm is calculated to be 761 and 2083 MPa, respectively, according to Eq. (8). For the aforementioned FG wrought-annealed CrMnFeCoNi alloy with grain size of 503 nm, the estimated twinning stress is surprisingly high and is not reached till fracture, and therefore the nanoscale deformation twins are not observed.

For our LENS^{TM}-deposited CrMnFeCoNi alloy, the estimated twinning stress of 761 MPa is reached at a lower logarithmic strain of ~13%. The earlier activation of the deformation twins in the LENS^{TM}-deposited CrMnFeCoNi alloy is believed to be a direct result of two opposite effects. The higher twinning stress and the lower work hardening rate of the LENS^{TM}-deposited CrMnFeCoNi alloy make it more difficult to generate twinning. However, this adverse effect is fully compensated by its higher yield strength (i.e. 517 MPa of the LENS^{TM}-deposited CrMnFeCoNi alloy vs 265 MPa of the wrought-annealed counterpart), which results in its earlier reaching of the twinning stress 761 MPa, at a lower logarithmic strain level. As discussed earlier, the formation of these nanoscale deformation twins introduces additional intragrain interfaces which act as “strong” obstacles for gliding dislocations, and the earlier activation of these deformation twins is undoubtedly desirable. We observe that, however, the onset of twinning in the LENS^{TM}-deposited CrMnFeCoNi alloy is

already very close to its necking instability point, i.e. 15.7% logarithmic strain, which implies that its uniform plastic deformation capability has been almost exhausted before the onset of twinning. Therefore, the lowered uniform tensile elongation of our LENS^{TM}-deposited CrMnFeCoNi alloy is believed to result from the evolution of dislocations (i.e. another work hardening contributor) during the course of straining.

4.3.4. The role of dislocation evolution in uniform tensile ductility

As can be seen by comparing Figs. 6 and 9, the dislocations are only slightly denser in the as-deformed microstructure of the LENS^{TM}-deposited CrMnFeCoNi alloy, which differs with the dramatically increased dislocation density reported for the wrought-annealed counterpart [8]. In other words, the net increase in the dislocation density during the straining process is smaller for the LENS^{TM}-deposited CrMnFeCoNi alloy as compared with the wrought-annealed counterpart. The evolution of the dislocation density during the straining process is concurrently determined by the accumulation and annihilation of the dislocations. According to a time-proven approach proposed by Kocks and Mecking [70-72], the evolution of the dislocation density with the strain, $d\rho/d\varepsilon$, can be estimated by:

$$d\rho/d\varepsilon = M(k_1\sqrt{\rho} - k_2\rho) \quad (9)$$

where the dislocation storage rate coefficient, k_1, is associated with the dislocation accumulation due to the dislocation-dislocation interactions (e.g. the interactions between the gliding dislocations and forest ones), and the dynamic recovery coefficient, k_2, is associated with the dislocation annihilation by several possible mechanisms (e.g. the climb of edge dislocations, and the cross-slip of screw dislocations). These two parameters k_1 and k_2 are microstructural dependent constants.

The increased dislocation density ρ would lead to an increased flow stress σ, as given by the Taylor equation (Eq. (3)), but the $\Delta\sigma_{DS}$ in Eq. (3) is substituted by the flow stress σ here [50]:

$$\sigma = M\alpha Gb\sqrt{\rho} \tag{10}$$

Combining Eqs. (9) and (10) provides the flow stress as a function of the strain in the plastic regime:

$$\sigma = (\alpha GbMk_1/k_2)\,[1 - exp(-k_2M\varepsilon/2)] \tag{11}$$

Eq. (11) satisfactorily describes a large amount of true stress-logarithmic strain experimental data in the plastic regime of conventional alloys with CG microstructures [73]. To extend Eq. (11) to FG or even UFG microstructures, the grain boundary strengthening needs to be considered, and therefore a grain size dependent constant σ_1 is suggested and introduced into Eq. (11) as follows [74]:

$$\sigma = \sigma_1 + (\alpha GbMk_1/k_2)\,[1 - exp(-k_2M\varepsilon/2)] \tag{12}$$

Eq. (12) can be used successfully to describe a variety of alloys over a wide range of grain sizes [75]. Going one step further, the plastic instability corresponding to the onset of the nonuniform plastic deformation is derived by linear stability analysis [73-75]:

$$(h/\sigma)\,(1 - 1/m) + [k_2M/(2m)]\,(1 - \sigma_1/\sigma) \leq 1 \tag{13}$$

where the parameter m is associated with but not exactly the strain rate sensitivity introduced by Hart [76]. The parameter h is the aforementioned work hardening rate and given by:

$$h = d\sigma/d\varepsilon = (\alpha GbM^2 k_1/2)\, exp(-k_2 M\varepsilon/2) \quad (14)$$

It can be seen from Eq. (14) that both the dislocation storage rate coefficient, k_1, and the dynamic recovery coefficient, k_2, affect the work hardening capability of an alloy. Nevertheless, we want to emphasize that the parameter k_2 exhibits a more pronounced effect because it resides in the exponential function. Replacing the flow stress, σ, and the strain hardening coefficient, h, in Ineq. (13) with the expressions in Eqs. (12) and (14), respectively, and substituting the equality sign for the inequality sign leads to the necking strain ε_N [73-75]:

$$\varepsilon_N = [2/(k_2 M)] \cdot \ln\{[1 + (k_2 M/2)(1 - 2/m)]/[1 + \sigma_1 k_2/(\alpha GbMk_1) - k_2 M/(2m)\} \quad (15)$$

For a variety of alloys and testing conditions, $1/m$ <<1, and therefore Eq. (15) can be reduced to:

$$\varepsilon_N = [2/(k_2 M)] \cdot \ln\{[1 + (k_2 M/2)]/[1 + \sigma_1 k_2/(\alpha GbMk_1)]\} \quad (16)$$

Eq. (16) can be used to estimate the onset of necking during the course of the monotonic tension. It can be again seen from Eq. (16) that the dynamic recovery rate coefficient k_2 governs the necking phenomenon. By contrast, the other intrinsic model variables, i.e. k_1 and σ_1, are less significant as they affect the necking strain logarithmically. To further highlight the important role of the parameter k_2 in the necking strain ε_N, the lower and the upper bound estimates based on Eq. (16) are given by:

$$2/(k_2 M) < \varepsilon_N < 2\ln[1 + k_2 M/2]/(k_2 M) \quad (17)$$

This double inequation is valid for any reasonable combinations of the model variables, and it clearly shows that the estimated necking true strain ε_N is in a very narrow band, with the upper and lower bounds governed by the k_2 value alone. The non-linear Eq. (12) is fitted to the measured true stress-logarithmic strain curve in the plastic regime, and very good fitting is achieved by adjusting the fitting parameters, i.e. the intrinsic model variables, as shown in Fig. 11. The necking true strain, ε_N, is estimated accordingly, based on Eq. (16), to be 16.2% which agrees well with the measured value 15.7%. Good fitting is also achieved for the wrought-annealed CrMnFeCoNi alloy, and the k_2 values for the LENS^{TM}-deposited and wrought-annealed CrMnFeCoNi alloys are 5.4 and 2.67, respectively. The larger k_2 value of the LENS^{TM}-deposited CrMnFeCoNi alloy indicates a promoted dynamic dislocation recovery process, and hence a less significant net increase in the dislocation density during straining, which is consistent with what we observed experimentally. As a direct result, the work hardening capability is somewhat weakened, which is believed to be the main reason for the reduced uniform tensile elongation of the LENS^{TM}-deposited CrMnFeCoNi alloy.

5. Conclusions

The primary goal of this study is to investigate the potential of the LENS^{TM} process in the manufacture of the equiatomic CrMnFeCoNi high entropy alloy. To investigate the potential, the CrMnFeCoNi alloy is additively manufactured by the LENS^{TM} process, and the solidification conditions, phase formation, as-deposited microstructures, and tensile behavior are investigated. Furthermore, the tensile yield strength and uniform tensile elongation are modeled, and the underlying mechanisms for the improved yield strength and lowered ductility, as compared with the

wrought-annealed counterparts with similar grain sizes, are discussed. The following conclusions could be drawn from our study:

(1) The LENS^{TM}-deposited CrMnFeCoNi alloy exhibits a single-phase disordered face centered cubic structure, as evidenced by XRD, and rationalized by Scheil's solidification simulation with the aid of the high entropy alloys database.

(2) Multi-scale as-deposited microstructures, i.e. columnar grains, solidification and dislocation substructures, are formed. Furthermore, elemental segregation is observed and rationalized by Scheil's simulation.

(3) The LENS^{TM}-deposited CrMnFeCoNi alloy exhibits a tensile yield strength that is comparable to that of finer-grained wrought-annealed counterparts. This is largely attributed to the high dislocation density, in the LENS^{TM}-deposited CrMnFeCoNi alloy, and hence the initial-dislocation strengthening, which are insignificant and can be disregarded in the wrought-annealed counterparts.

(4) The tensile deformation process is mainly accommodated by dislocation activities with the assistance of deformation twinning. The promoted dislocation recovery process during straining leads to a weakened work hardening capability, and hence a reduced uniform tensile elongation, as compared with the wrought-annealed counterparts. Overall, however, the capability of the LENS^{TM} process to manufacture the high-performance CrMnFeCoNi alloy for engineering applications is confirmed in this study.

Competing interests statement

The authors do not have competing interests.

Acknowledgements

This work was supported by the Research Committee of The Hong Kong Polytechnic University through the research student project (account code: G_RUHS). The authors also gratefully thank Dunyong Deng at Linköping University for useful discussions.

Data availability

The raw/processed data required to reproduce these findings cannot be shared at this time due to technical or time limitations.

References

[1] J.W. Yeh, S.K. Chen, S.J. Lin, J.Y. Gan, T.S. Chin, T.T. Shun, C.H. Tsau, S.Y. Chang, Nanostructured high-entropy alloys with multiple principal elements: Novel alloy design concepts and outcomes, Adv. Eng. Mater. 6 (2004) 299-303.

[2] B. Cantor, I.T.H. Chang, P. Knight, A.J.B. Vincent, Microstructural development in equiatomic multicomponent alloys, Mater. Sci. Eng. A 375-377 (2004) 213-218.

[3] Y.J. Zhou, Y. Zhang, Y.L. Wang, G.L. Chen, Solid solution alloys of AlCoCrFeNiTix with excellent room-temperature mechanical properties, Appl. Phys. Lett. 90 (2007) 181904.

[4] Y. Yu, J. Wang, J.S. Li, H.C. Kou, H.T. Duan, J. Li, W.M. Liu, Tribological behavior of AlCoCrCuFeNi and AlCoCrFeNi$Ti_{0.5}$ high entropy alloys under hydrogen peroxide solution against different counterparts, Tribol. Int. 92 (2015) 203-210.

[5] Y. Yu, J. Wang, J.S. Li, J. Yang, H.C. Kou, W.M. Liu, Tribological behavior of AlCoCrFeNi($Ti_{0.5}$) high entropy alloys under oil and MACs lubrication, J. Mater. Sci.

Technol. 32 (2016) 470-476.

[6] Z. Tang, T. Yuan, C.W. Tsai, J.W. Yeh, C.D. Lundin, P.K. Liaw, Fatigue behavior of a wrought $Al_{0.5}$CoCrCuFeNi two-phase high-entropy alloy, Acta Mater. 99 (2015) 247-258.

[7] M.A. Hemphill, T. Yuan, G.Y. Wang, J.W. Yeh, C.W. Tsai, A. Chuang, P.K. Liaw, Fatigue behavior of $Al_{0.5}$CoCrCuFeNi high entropy alloys, Acta Mater. 60 (2012) 5723-5734.

[8] G. Laplanche, A. Kostka, O.M. Horst, G. Eggeler, E.P. George, Microstructure evolution and critical stress for twinning in the CrMnFeCoNi high-entropy alloy, Acta Mater. 118 (2016) 152-163.

[9] F. Otto, A. Dlouhy, C. Somsen, H. Bei, G. Eggeler, E.P. George, The influences of temperature and microstructure on the tensile properties of a CoCrFeMnNi high-entropy alloy, Acta Mater. 61 (2013) 5743-5755.

[10] B. Gludovatz, A. Hohenwarter, D. Catoor, E.H. Chang, E.P. George, R.O. Ritchie, A fracture-resistant high-entropy alloy for cryogenic applications, Science 345 (2014) 1153-1158.

[11] S. Xiang, H. Luan, J. Wu, K.-F. Yao, J. Li, X. Liu, Y. Tian, W. Mao, H. Bai, G. Le, Q. Li, Microstructures and mechanical properties of CrMnFeCoNi high entropy alloys fabricated using laser metal deposition technique, J. Alloys Compd. 773 (2019) 387-392.

[12] W. Ji, W.M. Wang, H. Wang, J.Y. Zhang, Y.C. Wang, F. Zhang, Z.Y. Fu, Alloying behavior and novel properties of CoCrFeNiMn high-entropy alloy fabricated by

mechanical alloying and spark plasma sintering, Intermetallics 56 (2015) 24-27.

[13] Y. Liu, J.S. Wang, Q.H. Fang, B. Liu, Y. Wu, S.Q. Chen, Preparation of superfine-grained high entropy alloy by spark plasma sintering gas atomized powder, Intermetallics 68 (2016) 16-22.

[14] S.H. Joo, H. Kato, M.J. Jang, J. Moon, E.B. Kim, S.J. Hong, H.S. Kim, Structure and properties of ultrafine-grained CoCrFeMnNi high-entropy alloys produced by mechanical alloying and spark plasma sintering, J. Alloys Compd. 698 (2017) 591-604.

[15] H. Shahmir, J. He, Z. Lu, M. Kawasaki, T.G. Langdon, Effect of annealing on mechanical properties of a nanocrystalline CoCrFeNiMn high-entropy alloy processed by high-pressure torsion, Mater. Sci. Eng. A 676 (2016) 294-303.

[16] I.A. Ovid'ko, R.Z. Valiev, Y.T. Zhu, Review on superior strength and enhanced ductility of metallic nanomaterials, Prog. Mater Sci. 94 (2018) 462-540.

[17] E. Ma, Instabilities and ductility of nanocrystalline and ultrafine-grained metals, Scr. Mater. 49 (2003) 663-668.

[18] Y. Wang, M. Chen, F. Zhou, E. Ma, High tensile ductility in a nanostructured metal, Nature 419 (2002) 912.

[19] R.S. Amano, P.K. Rohatgi, Laser engineered net shaping process for SAE 4140 low alloy steel, Mater. Sci. Eng. A 528 (2011) 6680-6693.

[20] I. Palcic, M. Balazic, M. Milfelner, B. Buchmeister, Potential of laser engineered net shaping (LENS) technology, Mater. Manuf. Processes 24 (2009) 750-753.

[21] M. Tang, P.C. Pistorius, S. Narra, J.L. Beuth, Rapid Solidification: Selective

Laser Melting of AlSi10Mg, JOM 68 (2016) 960-966.

[22] R.D. Li, P.D. Niu, T.C. Yuan, P. Cao, C. Chen, K.C. Zhou, Selective laser melting of an equiatomic CoCrFeMnNi high-entropy alloy: Processability, non-equilibrium microstructure and mechanical property, J. Alloys Compd. 746 (2018) 125-134.

[23] Y.H. Zhou, Z.H. Zhang, Y.P. Wang, G. Liu, S.Y. Zhou, Y.L. Li, J. Shen, M. Yan, Selective laser melting of typical metallic materials: An effective process prediction model developed by energy absorption and consumption analysis, Addit. Manuf. 25 (2019) 204-217.

[24] Z.G. Zhu, Q.B. Nguyen, F.L. Ng, X.H. An, X.Z. Liao, P.K. Liaw, S.M.L. Nai, J. Wei, Hierarchical microstructure and strengthening mechanisms of a CoCrFeNiMn high entropy alloy additively manufactured by selective laser melting, Scr. Mater. 154 (2018) 20-24.

[25] Z. Qiu, C. Yao, K. Feng, Z. Li, P.K. Chu, Cryogenic deformation mechanism of CrMnFeCoNi high-entropy alloy fabricated by laser additive manufacturing process, Int. J. Lightweight Mater. Manuf. 1 (2018) 33-39.

[26] Z. Tong, X. Ren, J. Jiao, W. Zhou, Y. Ren, Y. Ye, E.A. Larson, J. Gu, Laser additive manufacturing of FeCrCoMnNi high-entropy alloy: Effect of heat treatment on microstructure, residual stress and mechanical property, J. Alloys Compd. 785 (2019) 1144-1159.

[27] Y. Chew, G.J. Bi, Z.G. Zhu, F.L. Ng, F. Weng, S.B. Liu, S.M.L. Nai, B.Y. Lee, Microstructure and enhanced strength of laser aided additive manufactured CoCrFeNiMn high entropy alloy, Mater. Sci. Eng. A 744 (2019) 137-144.

[28] X. Gao, Y. Lu, Laser 3D printing of CoCrFeMnNi high-entropy alloy, Mater. Lett. 236 (2019) 77-80.

[29] M. Laurent-Brocq, A. Akhatova, L. Perriere, S. Chebini, X. Sauvage, E. Leroy, Y. Champion, Insights into the phase diagram of the CrMnFeCoNi high entropy alloy, Acta Mater. 88 (2015) 355-365.

[30] W.H. Liu, Y. Wu, J.Y. He, T.G. Nieh, Z.P. Lu, Grain growth and the Hall-Petch relationship in a high-entropy FeCrNiCoMn alloy, Scr. Mater. 68 (2013) 526-529.

[31] F. Otto, A. Dlouhy, K.G. Pradeep, M. Kubenova, D. Raabe, G. Eggeler, E.P. George, Decomposition of the single-phase high-entropy alloy CrMnFeCoNi after prolonged anneals at intermediate temperatures, Acta Mater. 112 (2016) 40-52.

[32] E.J. Pickering, R. Muñoz-Moreno, H.J. Stone, N.G. Jones, Precipitation in the equiatomic high-entropy alloy CrMnFeCoNi, Scr. Mater. 113 (2016) 106-109.

[33] B. Schuh, F. Mendez-Martin, B. Voelker, E.P. George, H. Clemens, R. Pippan, A. Hohenwarter, Mechanical properties, microstructure and thermal stability of a nanocrystalline CoCrFeMnNi high-entropy alloy after severe plastic deformation, Acta Mater. 96 (2015) 258-268.

[34] G.P. Dinda, A.K. Dasgupta, J. Mazumder, Evolution of microstructure in laser deposited Al-11.28%Si alloy, Surf. Coat. Technol. 206 (2012) 2152-2160.

[35] G.P. Dinda, A.K. Dasgupta, J. Mazumder, Texture control during laser deposition of nickel-based superalloy, Scr. Mater. 67 (2012) 503-506.

[36] G.P. Dinda, A.K. Dasgupta, J. Mazumder, Laser aided direct metal deposition of Inconel 625 superalloy: Microstructural evolution and thermal stability, Mater. Sci.

Eng. A 509 (2009) 98-104.

[37] G.P. Dinda, A.K. Dasgupta, S. Bhattacharya, H. Natu, B. Dutta, J. Mazumder, Microstructural characterization of laser-deposited Al 4047 alloy, Metall. Mater. Trans. A 44A (2013) 2233-2242.

[38] Y.M. Ren, X. Lin, X. Fu, H. Tan, J. Chen, W.D. Huang, Microstructure and deformation behavior of Ti-6A1-4V alloy by high-power laser solid forming, Acta Mater. 132 (2017) 82-95.

[39] M. Gäumann, C. Bezencon, P. Canalis, W. Kurz, Single-crystal laser deposition of superalloys: Processing-microstructure maps, Acta Mater. 49 (2001) 1051-1062.

[40] S. Gorsse, C. Hutchinson, M. Goune, R. Banerjee, Additive manufacturing of metals: a brief review of the characteristic microstructures and properties of steels, Ti-6Al-4V and high-entropy alloys, Sci. Technol. Adv. Mat. 18 (2017) 584-610.

[41] C. Qiu, M.A. Kindi, A.S. Aladawi, I.A. Hatmi, A comprehensive study on microstructure and tensile behaviour of a selectively laser melted stainless steel, Sci. Rep. 8 (2018) 7785.

[42] L. Liu, Q. Ding, Y. Zhong, J. Zou, J. Wu, Y.-L. Chiu, J. Li, Z. Zhang, Q. Yu, Z. Shen, Dislocation network in additive manufactured steel breaks strength–ductility trade-off, Mater. Today 21 (2018) 354-361.

[43] D.Y. Deng, R.L. Peng, H. Brodin, J. Moverare, Microstructure and mechanical properties of Inconel 718 produced by selective laser melting: Sample orientation dependence and effects of post heat treatments, Mater. Sci. Eng. A 713 (2018) 294-306.

[44] J. Chen, Z. Yao, X. Wang, Y. Lu, X. Wang, Y. Liu, X. Fan, Effect of C content on microstructure and tensile properties of as-cast CoCrFeMnNi high entropy alloy, Mater. Chem. Phys. 210 (2018) 136-145.

[45] G.A. Salishchev, M.A. Tikhonovsky, D.G. Shaysultanov, N.D. Stepanov, A.V. Kuznetsov, I.V. Kolodiy, A.S. Tortika, O.N. Senkov, Effect of Mn and V on structure and mechanical properties of high-entropy alloys based on CoCrFeNi system, J. Alloys Compd. 591 (2014) 11-21.

[46] J. Friedel, Dislocations, New York, Pergamon Press, 1964.

[47] V. Mohles, Simulations of dislocation glide in overaged precipitation-hardened crystals, Philos. Mag. A 81 (2001) 971-990.

[48] S.J. Sun, Y.Z. Tian, H.R. Lin, X.G. Dong, Y.H. Wang, Z.J. Zhang, Z.F. Zhang, Enhanced strength and ductility of bulk CoCrFeMnNi high entropy alloy having fully recrystallized ultrafine-grained structure, Mater. Des. 133 (2017) 122-127.

[49] Y.J. Yin, J.Q. Sun, J. Guo, X.F. Kan, D.C. Yang, Mechanism of high yield strength and yield ratio of 316 L stainless steel by additive manufacturing, Materials Science and Engineering: A 744 (2019) 773-777.

[50] G.I. Taylor, The mechanism of plastic deformation of crystals. Part I.—Theoretical, Proc. R. Soc. Lond. A 145 (1934) 362.

[51] R.E. Stoller, S.J. Zinkle, On the relationship between uniaxial yield strength and resolved shear stress in polycrystalline materials, J. Nucl. Mater. 283-287 (2000) 349-352.

[52] Z. Wu, H. Bei, G.M. Pharr, E.P. George, Temperature dependence of the

mechanical properties of equiatomic solid solution alloys with face-centered cubic crystal structures, Acta Mater. 81 (2014) 428-441.

[53] G. Laplanche, P. Gadaud, O. Horst, F. Otto, G. Eggeler, E.P. George, Temperature dependencies of the elastic moduli and thermal expansion coefficient of an equiatomic, single-phase CoCrFeMnNi high-entropy alloy, J. Alloys Compd. 623 (2015) 348-353.

[54] Q. Lin, X. An, H. Liu, Q. Tang, P. Dai, X. Liao, In-situ high-resolution transmission electron microscopy investigation of grain boundary dislocation activities in a nanocrystalline CrMnFeCoNi high-entropy alloy, J. Alloys Compd. 709 (2017) 802-807.

[55] Y.H. Zhao, X.Z. Liao, Z. Jin, R.Z. Valiev, Y.T. Zhu, Microstructures and mechanical properties of ultrafine grained 7075 Al alloy processed by ECAP and their evolutions during annealing, Acta Mater. 52 (2004) 4589-4599.

[56] S. Kumari, D.K. Singh, P.K. Giri, Strain anisotropy in freestanding germanium nanoparticles synthesized by ball milling, J. Nanosci. Nanotechnol. 9 (2009) 5231-5236.

[57] G.K. Williamson, R.E. Smallman, III. Dislocation densities in some annealed and cold-worked metals from measurements on the X-ray debye-scherrer spectrum, Philos. Mag. 1 (1956) 34-46.

[58] D. Wang, C. Song, Y. Yang, Y. Bai, Investigation of crystal growth mechanism during selective laser melting and mechanical property characterization of 316L stainless steel parts, Mater. Des. 100 (2016) 291-299.

[59] G.P. Dinda, L. Song, J. Mazumder, Fabrication of Ti-6Al-4V scaffolds by direct

metal deposition, Metall. Mater. Trans. A 39 (2008) 2914-2922.

[60] H. Ali, H. Ghadbeigi, K. Mumtaz, Processing parameter effects on residual stress and mechanical properties of selective laser melted Ti6Al4V, J. Mater. Eng. Perform. 27 (2018) 4059-4068.

[61] A. Considère, Mémoire sur l'emploi du fer et de l'acier dans les constructions, Ann des Ponts et Chaussés (1885) 574-775.

[62] K. Lu, L. Lu, S. Suresh, Strengthening materials by engineering coherent internal boundaries at the nanoscale, Science 324 (2009) 349.

[63] M.A. Meyers, O. Vöhringer, V.A. Lubarda, The onset of twinning in metals: a constitutive description, Acta Mater. 49 (2001) 4025-4039.

[64] K.M. Rahman, V.A. Vorontsov, D. Dye, The effect of grain size on the twin initiation stress in a TWIP steel, Acta Mater. 89 (2015) 247-257.

[65] I. Gutierrez-Urrutia, D. Raabe, Grain size effect on strain hardening in twinning-induced plasticity steels, Scr. Mater. 66 (2012) 992-996.

[66] I. Gutierrez-Urrutia, S. Zaefferer, D. Raabe, The effect of grain size and grain orientation on deformation twinning in a Fe–22wt.% Mn–0.6wt.% C TWIP steel, Mater. Sci. Eng. A 527 (2010) 3552-3560.

[67] A.J. Zaddach, C. Niu, C.C. Koch, D.L. Irving, Mechanical properties and stacking fault energies of NiFeCrCoMn high-entropy alloy, JOM 65 (2013) 1780-1789.

[68] S. Huang, W. Li, S. Lu, F. Tian, J. Shen, E. Holmström, L. Vitos, Temperature dependent stacking fault energy of FeCrCoNiMn high entropy alloy, Scr. Mater. 108

(2015) 44-47.

[69] Y.T. Zhu, X.Z. Liao, X.L. Wu, J. Narayan, Grain size effect on deformation twinning and detwinning, J. Mater. Sci. 48 (2013) 4467-4475.

[70] U.F. Kocks, Laws for work-hardening and low-temperature creep, J. Eng. Mater. Tech. Trans. ASME 98 (1976) 76-85.

[71] H. Mecking, U.F. Kocks, Kinetics of flow and strain-hardening, Acta Metall. 29 (1981) 1865-1875.

[72] Y. Estrin, H. Mecking, A unified phenomenological description of work hardening and creep based on one-parameter models, Acta Metall. 32 (1984) 57-70.

[73] I.S. Yasnikov, A. Vinogradov, Y. Estrin, Revisiting the Considère criterion from the viewpoint of dislocation theory fundamentals, Scr. Mater. 76 (2014) 37-40.

[74] A. Vinogradov, I.S. Yasnikov, H. Matsuyama, M. Uchida, Y. Kaneko, Y. Estrin, Controlling strength and ductility: Dislocation-based model of necking instability and its verification for ultrafine grain 316L steel, Acta Mater. 106 (2016) 295-303.

[75] A. Vinogradov, Mechanical properties of ultrafine-grained metals: New challenges and perspectives, Adv. Eng. Mater. 17 (2015) 1710-1722.

[76] E.W. Hart, Theory of the tensile test, Acta Metall. 15 (1967) 351-355.